Numerical simulations of vibration in phase-shifting interferometry

Peter J. de Groot and Leslie L. Deck

Computer simulations predict the expected rms measurement error in a phase-shifting interferometer in the presence of mechanical vibrations. The simulations involve a numerical resolution of a nonlinear mathematical model and are performed over a range of vibrational frequencies and amplitudes for three different phase-shift algorithms. Experimental research with an interference microscope and comparison with analytical solutions verify the numerical model. © 1996 Optical Society of America

1. Introduction

One of the less fortunate characteristics of phase-shifting interferometry (PSI) is its sensitivity to mechanical vibration. Sensitivity to vibration is a fundamental limitation of the technique, and it is important to understand and quantify the error propagation through data-processing algorithms. Although a great deal of research has gone into characterizing PSI as a function for a variety of error sources,[1–4] there is comparatively little available literature on the effects of vibration.

A recent analytical study showed that a linear systems theory can predict the phase-measurement error in PSI in the limit of small vibrational amplitudes.[5] The analytical approach shows that it is possible to suppress errors caused by vibration through the appropriate choice of PSI algorithm and data-acquisition rate. However, a linear approximation is valid only for small vibrations, and therefore it does not completely characterize the behavior of PSI systems in the presence of many important forms of environmental noise. Higher-order nonlinear approximations are possible but are considerably more complicated.

A general approach to quantifying vibration is through the numerical resolution of a complete, nonlinear mathematical model of PSI with a well-defined vibration. A numerical simulation has the advantage that it can cover a wider range of situations than analytical methods based on a linear approximation. On the one hand, numerical methods can justly be criticized for not providing any physical insight into the problem. On the other hand, a more sophisticated analysis will generally be checked against a numerical simulation to verify its validity.

We propose, therefore, a numerical algorithm for a computer-simulated PSI system in the presence of mechanical vibration. The principal objectives of the numerical calculations are to better define the limits of the analytical approach of Ref. 5 and to determine when PSI fails because of mechanical vibration during the measurement. After presenting the mathematical model and its numerical analog, we apply the model to three common PSI algorithms over a range of vibrational frequencies and amplitudes. We conclude with an experimental confirmation of the accuracy of the model that uses an interference microscope and a controlled source of vibration.

2. Mathematical Model

Most often, the objective of PSI in optical testing is to determine surface figures from an amplitude-division interference pattern. The PSI software estimates interferometric phase θ at each point on the object surface by processing the variation of intensity as a function of time, during a linear shift in the phase.[6] The time-dependent signal for a given image point or pixel in the field of view may be written as

$$g(\theta, t) = Q[1 + V\cos[\theta + \phi(t)]], \quad (1)$$

The authors are with the Zygo Corporation, Laurel Brook Road, Middlefield, Connecticut 06455.

Received 12 June 1995; revised manuscript received 20 November 1995.

0003-6935/96/132172-07$10.00/0

© 1996 Optical Society of America

where V is the fringe visibility, Q is a constant, and $\phi(t)$ is the phase shift. One common way of introducing a time-dependent phase shift uniformly over the entire field of view is by precise mechanical displacement of the reference surface.

Instrumentation for surface-measuring PSI often includes a sensor array such as a CCD camera. The sensor array acquires J frames of data and transmits them to a computer for processing. In the integrating-bucket technique for PSI, the data are acquired during a linear phase shift

$$\phi(t) = 2\pi v_0 t, \tag{2}$$

at a frequency v_0, and the intensity data for each frame are integrated over a time period

$$\tau = \frac{\beta}{2\pi v_0}, \tag{3}$$

where β is the nominal phase shift between data frames or buckets. The integrated intensities $\bar{g}_j$ for data frames $j = 0 \ldots J - 1$ are therefore

$$\bar{g}_j = \frac{1}{\tau}\int_{-\tau/2}^{+\tau/2} g(\theta, t_j + t')\mathrm{d}t', \tag{4}$$

where

$$t_j = j\tau. \tag{5}$$

The integrating-bucket method simplifies the phase-shift procedure and reduces the sensitivity of the instrument to high-frequency noise.

The PSI data analysis algorithm is typically of the form

$$\varphi = \tan^{-1}(T) + \text{const}, \tag{6}$$

where

$$T = \sum_{j=0}^{J-1} s_j \bar{g}_j \Big/ \sum_{j=0}^{J-1} c_j \bar{g}_j \tag{7}$$

and coefficients s_j, c_j are characteristic of the particular PSI algorithm. For example, a simple three-bucket algorithm using a $\beta = \pi/2$ phase-shift interval has the form[7]

$$T = \frac{\bar{g}_3 - \bar{g}_2}{\bar{g}_1 - \bar{g}_2}. \tag{8}$$

There are currently a wide variety of alternative algorithms that use anywhere from three to 15 data frames. If the system is free of all noise sources, measured phase φ will be identical to actual phase θ.

During a PSI acquisition, mechanical vibrations $n(t)$ will be added to the linear motion of the phase modulator, resulting in a distorted intensity signal $g'(\theta, t)$:

$$g'(\theta, t) = Q[1 + V\cos[\phi(t) + \theta - n(t)]]. \tag{9}$$

The mathematical model as outlined so far is not restricted to any particular form of vibrational noise. However, to gain some insight into the behavior of the system, we find it useful to consider the effects of pure vibrational tones of frequency v, amplitude A, and phase offset α. Thus

$$n(t) = A\cos(2\pi v t + \alpha). \tag{10}$$

In the linear approximation, it is possible for us to calculate the error caused by a complicated vibration by summing the contributions from each of the frequency components of the vibration.[5] In the more general situation to be considered in Section 3, the vibrational amplitudes may be large enough to introduce significant nonlinear coupling between frequency components. Thus the sensitivity of PSI to a particular vibrational frequency cannot be extrapolated to more complicated situations involving several vibrational tones. Nonetheless, a breakdown by frequency is perhaps the most readily comprehensible characterization of a PSI system in the presence of vibration.

Phase error $\Delta\varphi = \varphi - \theta$ is a function of a number of parameters, including the actual phase θ that we are trying to measure. It is the θ dependency that is most damaging to surface measurements, because it appears as a sinusoidal distortion or ripple artifact at twice the frequency of the interference fringes.[8] The magnitude of the error depends on amplitude A, frequency v, and phase α of the vibration [cf. Eq. (10)]. In practice, we often know something about the frequency content of vibrational noise in a given environment, but the phase information is unknown or random. In this case it is preferable to express the phase error in terms of a root-mean-square (rms) expectation. This is the number we would expect to obtain experimentally after calculating the rms phase error for a large number of measurements in the presence of a random vibration. The objective of the mathematical model is therefore to provide an estimate, E, of the rms ripple distortion as a function of vibrational frequency, averaged over all phase angles θ and α. For a given amplitude A and frequency v, the rms error is

$$E = \frac{1}{2\pi}\left(\int_{-\pi}^{\pi}\int_{-\pi}^{\pi}\{\Delta\varphi(\theta, \alpha) - \text{ave}[\Delta\varphi(\alpha)]\}^2\mathrm{d}\theta\mathrm{d}\alpha\right)^{1/2}, \tag{11}$$

where

$$\text{ave}[\Delta\varphi(\alpha)] = \frac{1}{2\pi}\int_{-\pi}^{\pi}\Delta\varphi(\theta, \alpha)\mathrm{d}\theta. \tag{12}$$

The objective of this paper is to evaluate these integrals numerically.

3. Numerical Simulation

The simplest numerical solution to the equations presented in Section 2 is to replace the integrals with discrete sums and to process these sums in sequence

by the use of a desktop computer. This is exactly what we propose to do. We therefore make no claim to efficiency in the execution of the calculations, which can take as long as 1 h to complete over a range of 60 vibrational frequencies.

The intensity formula for the numerical simulation is

$$g(\theta, \alpha, t) = Q[1 + V\cos[\phi(t) + \theta - A\cos(2\pi\nu t + \alpha)]]. \tag{13}$$

The integrating effect corresponding to Eq. (4) is simulated with the average of N closely spaced intensity calculations within each integrating period τ:

$$\bar{g}_j(\theta, \alpha) = \sum_{n=0}^{N-1} g(\theta, \alpha, t_j + t_n), \tag{14}$$

where

$$t_n = \left(n - \frac{N-1}{2}\right)\frac{\tau}{N}. \tag{15}$$

The phase error caused by vibration is

$$\Delta\varphi(\theta, \alpha) = \varphi(\theta, \alpha) - \theta, \tag{16}$$

where

$$\varphi = \tan^{-1}[T(\theta, \alpha)] + \text{const}, \tag{17}$$

$$T(\theta, \alpha) = \sum_{j=0}^{J-1} s_j\bar{g}_j(\theta, \alpha)\Big/\sum_{j=0}^{J-1} c_j\bar{g}_j(\theta, \alpha). \tag{18}$$

Finally, the discrete formula for numerically calculating rms ripple error E caused by vibrational noise is

$$E = \left(\frac{1}{K}\frac{1}{M}\sum_{k=0}^{K-1}\sum_{m=0}^{M-1}[\Delta\varphi(\alpha_k, \theta_m) - \text{ave}[\Delta\varphi(\alpha_k)]]^2\right)^{1/2}, \tag{19}$$

where

$$\text{ave}[\Delta\varphi(\alpha_k)] = \frac{1}{M}\sum_{m=0}^{M-1}\Delta\varphi(\alpha_k, \theta_m). \tag{20}$$

Phases θ_m are incremented over a $-\pi < \theta_m \le \pi$ range in M equal steps. Vibrational phase angles α_k are also incremented over a $-\pi < \alpha_k \le \pi$ range in K equal steps.

4. Results

We have applied the numerical simulation to three different PSI algorithms over a range of vibrational frequencies and amplitudes. The three algorithms all use a phase-shift interval $\beta = \pi/2$, and the vibrational frequencies have been normalized to ν_0, which in this case is one fourth of the camera frame rate. Thus a vibrational frequency of 50 Hz with a camera rate of 25 Hz is normalized to 8. The amplitude of the vibration as well as the expected rms error are expressed in units of fringes, where one fringe is equal to 2π rad of phase. The discrete sums in Eqs. (14), (19), and (20) were performed with $K = M = N = 15$.

The three graphs in Fig. 1 show the results of the numerical simulations for the three-bucket algorithm [Eq. (8)]. The same graphs include the analytical solution (Appendix A). The graphs show that the small-amplitude approximation needed for the analytical approach is valid up to amplitudes of $1/10$ fringe but is less useful for stronger vibrations. However, both the analytical and numerical solutions show a strong variation in sensitivity as a function of vibrational frequency, and both solutions show peak sensitivities at the same frequencies.

We have also applied the numerical solution to the five-bucket algorithm recently introduced by Schmit and Creath.[9] The algorithm has the form

$$T = \frac{(\bar{g}_5 - \bar{g}_1) + 4(\bar{g}_2 - \bar{g}_4)}{(\bar{g}_1 + \bar{g}_5) + 2(\bar{g}_2 + \bar{g}_4) - 6\bar{g}_3}. \tag{21}$$

Figure 2 shows the frequency dependency of the expected error as a function of vibrational frequency. The Schmit–Creath five-bucket algorithm is considerably less sensitive to vibration than the three-bucket algorithm.

As a final example, we ran simulations of a seven-bucket algorithm[10] having the form

$$T = \frac{(\bar{g}_0 - \bar{g}_6) - 7(\bar{g}_2 - \bar{g}_4)}{4(\bar{g}_1 + \bar{g}_5) - 8\bar{g}_3}. \tag{22}$$

This algorithm is also highly resistant to calibration errors and nonlinearities in the phase shift and has improved vibration resistance with respect to both the three- and five-bucket algorithms. Here again, the numerical simulations closely follow the analytical result for vibrational amplitudes up to $1/10$ fringe, with the one exception of the null at a normalized vibrational frequency of one (see Fig. 3). The null is reproduced in the numerical simulation only at very small vibrational amplitudes of the order of $1/50$ fringe.

A general conclusion from these simulations is that the analytical approach of Ref. 5 provides a lower limit to the expected rms error, and that reality is almost always worse. The measurement degrades in accuracy above amplitudes of $1/10$ fringe much more rapidly than the linear approximation predicts. To pursue this point further, we ran several simulations with a vibrational amplitude of $1/2$ fringe. This is so large that only low-frequency vibrations are tolerated by the PSI system. Figure 4 shows the evolution of the failure as a function of frequency for three different algorithms, i.e., the three-bucket, the five-bucket, and the seven-bucket algorithm. The five- and seven-bucket algorithms

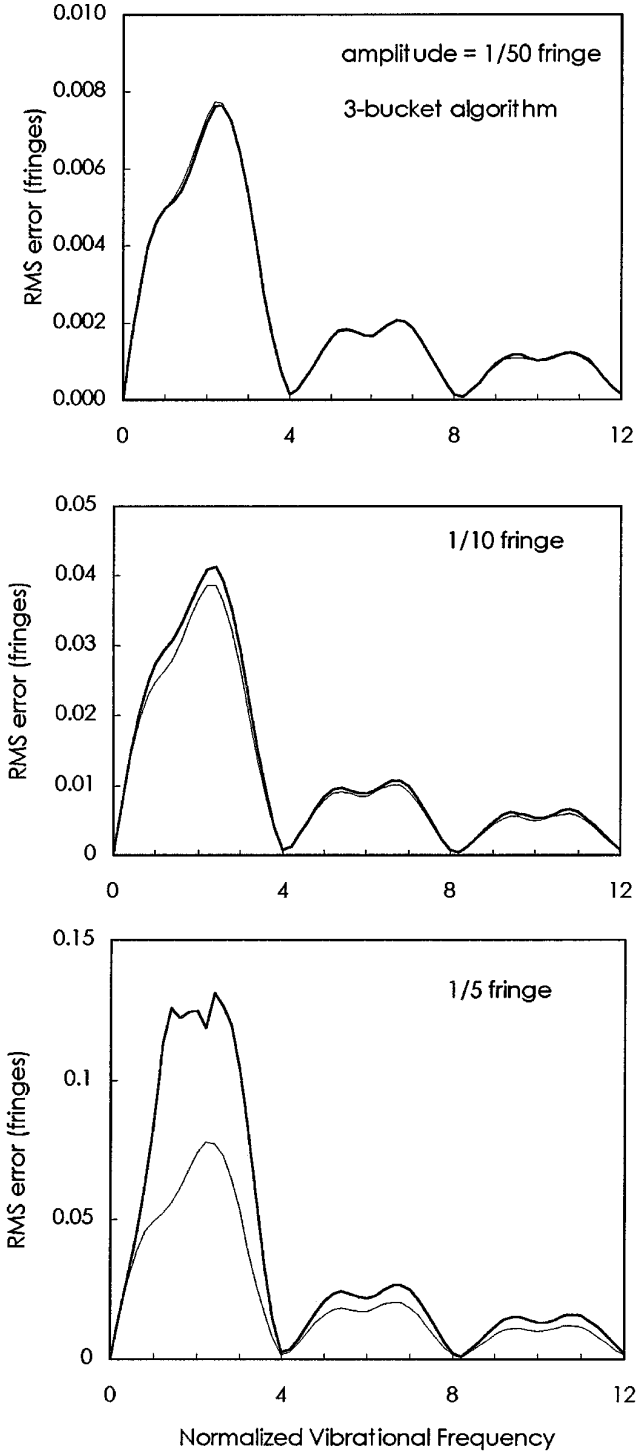

Fig. 1. Expected rms measurement error averaged over all phase angles for the three-bucket algorithm. The vibrational frequencies are normalized to $1/4$ of the camera frame rate. The lower curve in each graph is the analytical prediction based on the linear approximation of Ref. 5.

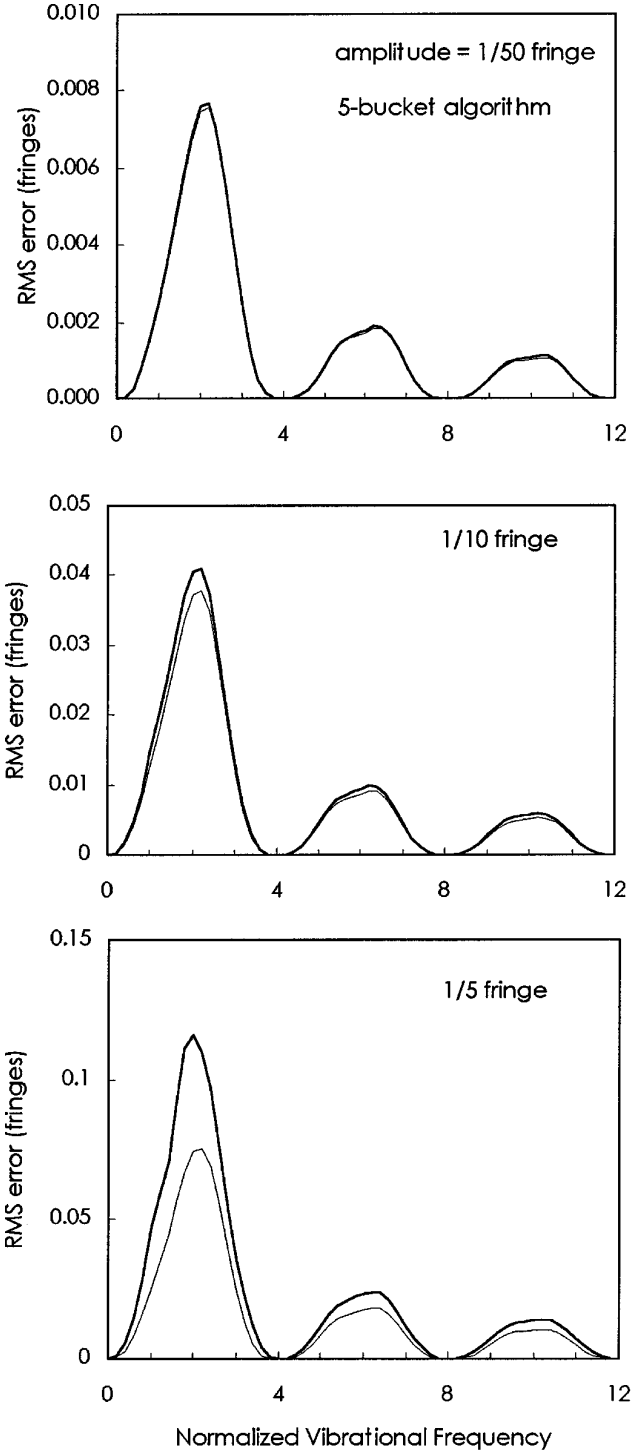

Fig. 2. Expected measurement error averaged over all phase angles for the Schmit–Creath five-bucket algorithm.

have much better low-frequency behavior than does the three-bucket algorithm, even for this relatively large vibrational amplitude. However, all three algorithms fail catastrophically ($E > 0.2$ fringe) at approximately the same vibrational frequency.

5. Experimental Verification

The numerical simulation has been carefully compared with experimental data to verify its validity. The instrument shown in Fig. 5 is a conventional interference microscope with a Mirau objective, and the object is an optical flat adjusted so as to provide two or three interference fringes across the field. The object is supported by a piezoelectric transducer

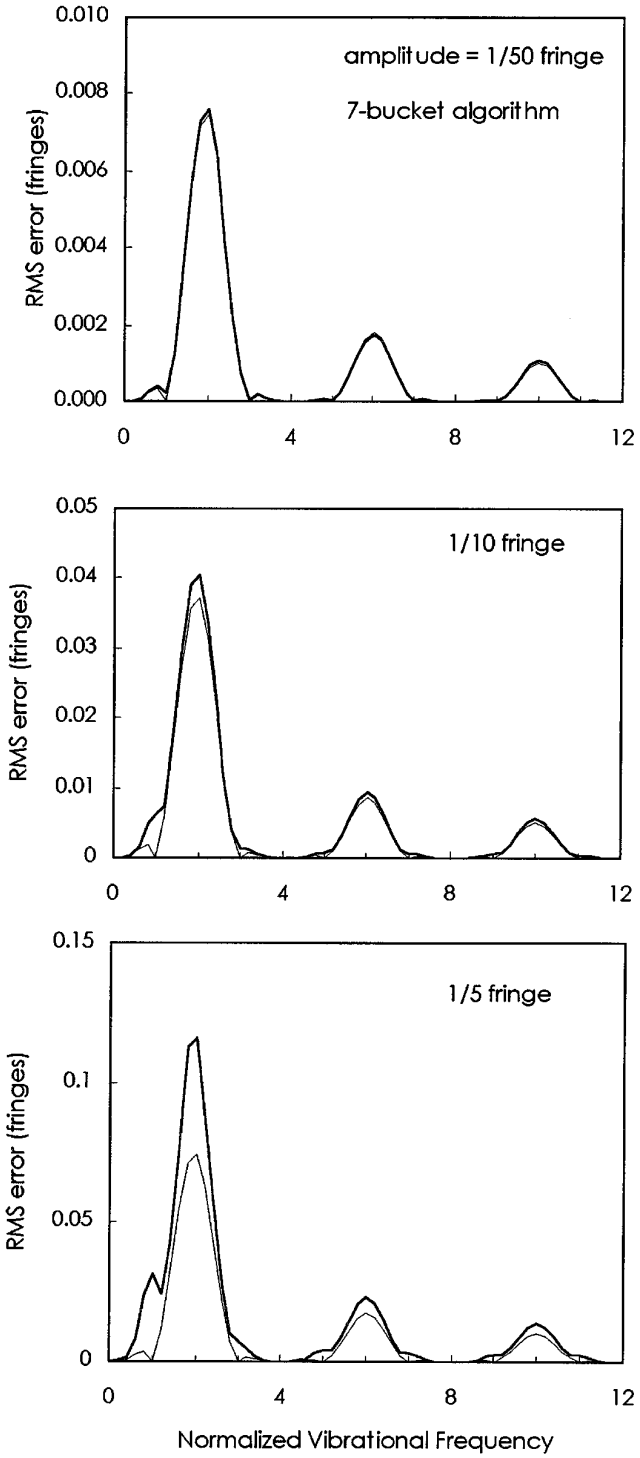

Fig. 3. Expected measurement error averaged over all phase angles for the seven-bucket algorithm.

(PZT) device driven by a waveform generator. The experimental procedure is to set the vibrational frequency and amplitude for pure sinusoidal vibrations and to acquire a sequence of ten phase images. The rms difference between these images is the measurement error caused by vibration.

The experiment was carried out on the seven-bucket algorithm over a range of vibrational frequencies and compared with the numerical simulation described in Section 4 for a vibrational amplitude of 1/4 fringe. The vibrational amplitude defined in this way is determined experimentally by observation of the interference fringe motion with the phase

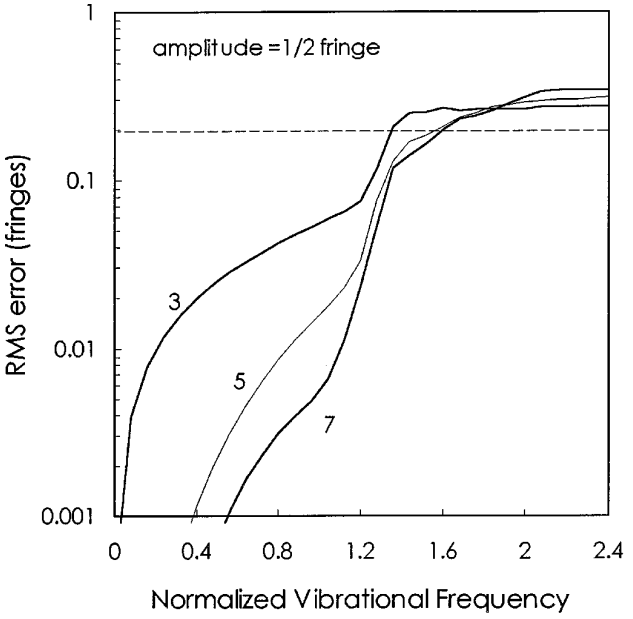

Fig. 4. Measurement error as a function of vibrational frequency for the three-, five-, and seven-bucket algorithms and a vibrational amplitude of 1/2 fringe. Although there are significant differences between the algorithms below a normalized frequency of one, all fail catastrophically above this frequency.

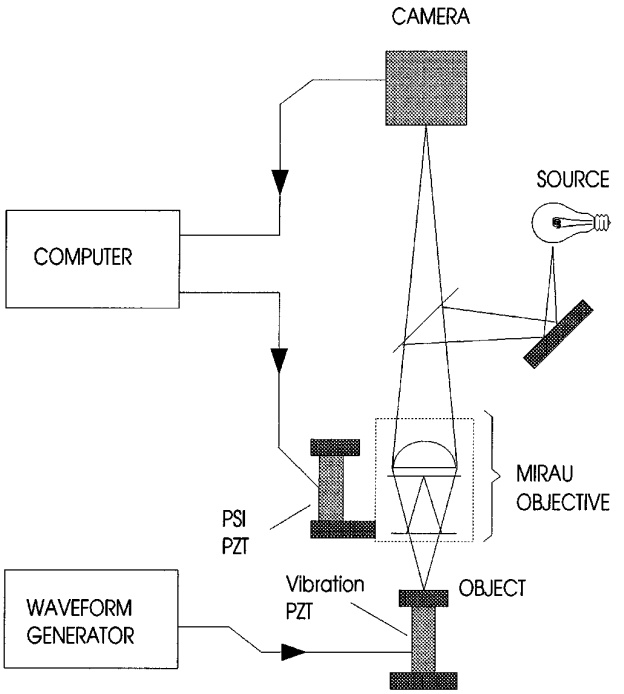

Fig. 5. Experimental system for verifying the numerical simulation. The waveform generator and PZT provide controlled mechanical vibrations.

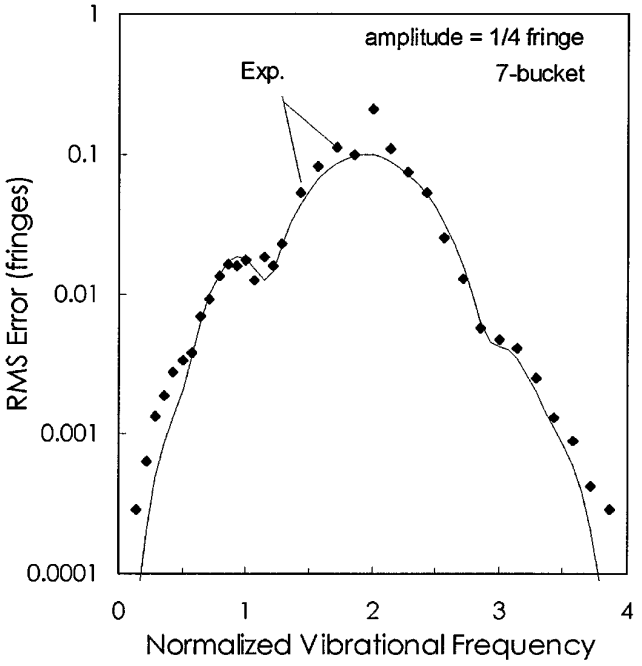

Fig. 6. Comparison of experimental and numerical simulations of vibrational errors in the seven-bucket algorithm.

shifter off and the vibration on. The data in Fig. 6 validate the appropriateness of the numerical simulation, at least for this experimental system.

We conclude therefore that the numerical simulation outlined in this paper is an accurate and useful representation of the behavior of PSI systems in the presence of vibration. The numerical and analytical solutions are in perfect agreement in the limit of low-amplitude vibrations, and experimental research verifies the accuracy of the numerical solution for the more general case.

Appendix A. Analytical Solutions

According to Ref. 5, the expected rms cyclic error of a PSI algorithm for a mechanical vibration of amplitude A, frequency v, and random phase is

$$E'(v) = \tfrac{1}{2}A|P_1(v) + P_2(v)|, \tag{A1}$$

where

$$P_1(v) = \tfrac{1}{4}[-F_C^*(v+1) - F_C^*(v-1) + i[F_S^*(v+1) - F_S^*(v-1)]], \tag{A2}$$

$$P_2(v) = \tfrac{1}{4}[-F_S^*(v+1) - F_S^*(v-1) - i[F_C^*(v+1) - F_C^*(v-1)]], \tag{A3}$$

and $F_S(v)$, $F_C(v)$ are the Fourier transforms of the numerator and denominator of a PSI algorithm. Frequency v is normalized to data-acquisition rate v_0, which for $\pi/2$ algorithms is $1/4$ the camera rate.

Equations (A1)–(A3) can also be combined into

$$E'(v) = \frac{A\sqrt{2}}{8}\,|i[F_S^*(v+1) + F_C^*(v-1)] - [F_S^*(v-1) + F_C^*(v+1)]|. \tag{A4}$$

If the PSI algorithm has the form

$$\theta = \tan^{-1}\left(\sum_{j=0}^{J-1} s_j\bar{g}_j \Big/ \sum_{j=0}^{J-1} c_j\bar{g}_j\right) \tag{A5}$$

and includes an integrating bucket of length β, then

$$F_S(\hat{v}) = H_S(\hat{v})B(\hat{v}),$$
$$F_C(\hat{v}) = H_C(\hat{v})B(\hat{v}), \tag{A6}$$

where

$$H_S(\hat{v}) = \frac{1}{q}\sum_j s_j \exp(-i\phi_j\hat{v}),$$

$$H_C(\hat{v}) = \frac{1}{q}\sum_j c_j \exp(-i\phi_j\hat{v}), \tag{A7}$$

$$q = \sum_j s_j \sin(-\phi_j) = \sum_j c_j \cos(\phi_j), \tag{A8}$$

$$B_v = \frac{\sin(v\beta/2)}{v\sin(\beta/2)}. \tag{A9}$$

The analytical solutions for the three-, five-, and seven-bucket algorithms considered in this paper are, respectively,

$$E_3'(v) = \frac{A}{2\sqrt{2}}\sin\left(\frac{v\pi}{4}\right) \times \left[(B_{v+1}{}^2 + B_{v-1}{}^2) + (B_{v+1}{}^2 - B_{v-1}{}^2)\sin\left(\frac{v\pi}{2}\right)\right]^{1/2}, \tag{A10}$$

$$E_5'(v) = \frac{A\sqrt{2}}{64}\left|(B_{v+1} - iB_{v-1}) \times \left[8\cos\left(\frac{v\pi}{2}\right) - 2\cos(v\pi) - 6\right] + (B_{v+1} + iB_{v-1})\left[-4\sin\left(\frac{v\pi}{2}\right) + 2\sin(v\pi)\right]\right|, \tag{A11}$$

$$E_7'(v) = A\left[\frac{1}{2}(B_{v+1}{}^2 + B_{v-1}{}^2)\right]^{1/2}\left|\frac{1}{2}\cos\left(\frac{v\pi}{2}\right)\sin^2\left(\frac{v\pi}{4}\right) + \frac{1}{32}\left[\cos\left(\frac{3v\pi}{2}\right) - \cos\left(\frac{v\pi}{2}\right)\right]\right|. \tag{A12}$$

These equations correspond to the thin curves in Figs. 1–3.

References

1. K. Kinnstätter, Q. W. Lohmann, J. Schwider, and N. Streibl, "Accuracy of phase shifting interferometry," Appl. Opt. **27,** 5082–5089 (1988).
2. L. A. Selberg, "Interferometer accuracy and precision," in *Optical Fabrication and Testing,* D. R. Campbell, C. W. Johnson, and M. Lorenzen, eds., Proc. Soc. Photo-Opt. Instrum. Eng. **1400,** 24–32 (1990).
3. J. van Wingerden, H. H. Frankena, and C. Smorenburg, "Linear approximation for measurement errors in phase shifting interferometry," Appl. Opt. **30,** 2718–2729 (1991).
4. K. Creath, "Comparison of phase-measurement algorithms," in *Surface Characterization and Testing,* K. Creath, ed., Proc. Soc. Photo-Opt. Instrum. Eng. **680,** 19–28 (1986).
5. P. de Groot, "Vibration in phase shifting interferometry," J. Opt. Soc. Am. A **12,** 354–365 (1995); "Errata," **12,** 2212 (1995).
6. J. E. Greivenkamp and J. H. Bruning, "Phase shifting interferometry," in *Optical Shop Testing,* D. Malacara, ed. (Wiley, New York, 1992), Chap. 14.
7. J. C. Wyant, C. L. Koliopoulos, B. Bushan, and O. E. George, "An optical profilometer for surface characterization of magnetic media," ASLE Trans. **27,** 101–105 (1984).
8. J. Schwider, "Phase shifting interferometry: reference phase error reduction," Appl. Opt. **28,** 3889–3892 (1989).
9. J. Schmit and K. Creath, "Some new error-compensating algorithms for phase-shifting interferometry," in *Optical Fabrication and Testing,* Vol. 13 of 1994 OSA Technical Digest Series (Optical Society of America, Washington, D.C., 1994), postdeadline paper PD-4.
10. P. de Groot, "Long-wavelength laser diode interferometer for surface flatness measurement," in *Optical Measurements and Sensors for the Process Industries,* C. Gorecki, and R. W. Preater, eds., Proc. Soc. Photo-Opt. Instrum. Eng. **2248,** 136–140 (1994).